Orbital Debris Shape Effect Investigations for Mitigating Risk

Heather Cowardin[1]

[1] NASA Orbital Debris Program Office, NASA Johnson Space Center,

Eric Christiansen[2], Mark Matney[1], Joshua Miller[3], Bruce (Alan) Davis[4] Corbin Cruz[4], John Seago[4], Austen King[4], John Opiela[4], Alyssa Manis[1]

[2] NASA Johnson Space Center, Hypervelocity Impact Technology, [3]University of Texas at El Paso
[4]Jacobs Technology, JETS

ABSTRACT

NASA's Orbital Debris Program Office (ODPO) and Hypervelocity Impact Technology (HVIT) team have coordinated to better understand the risks to upper stages and spacecraft from non-spherical orbital debris. It is well understood that fragmentation (collision or explosion) events in orbit produce fragments of various materials, sizes, and shapes. To further characterize these parameters, the ODPO is developing the next-generation Orbital Debris Engineering Model (ORDEM) version 4.0 to include orbital debris shape distributions. Ground-based assets, such as radar and optical sensors, can provide size estimates and some insight into material based on radar return or optical filter photometry/spectroscopy, respectively. Characterizing an object's shape requires more laboratory analyses to infer how shape affects these measurements. More importantly, in addition to size and material/density, the shape of fragments in orbit will alter the ballistic limit equations used in orbital debris risk assessments with NASA's Bumper Code. The ODPO plans to release ORDEM 4.0 in the coming years.

Performing ground-based laboratory impact tests on high-fidelity spacecraft mockups provides the means to directly measure size, mass, material/density, and shape of fragments, all key parameters needed to characterize real-world break up events. The DebriSat test, the results of which are provided, showcases the details of this type of experiment. The goal of this collaborative research between the ODPO and the HVIT team is to include a shape parameter in the environmental and breakup models used to assess risk for various space structures.

This paper examines ground-based laboratory impact tests and the associated fragment shape categories. Provided these defined shapes, the approach is simplified by assuming a right circular cylinder (RCC) approximation with varying length-to-diameter ratios. Highlights of impact tests conducted by the HVIT team using non-spherical projectiles based on the RCC approximation are presented. Hydrocode simulations have also been performed to expand on the complexity of variations with non-spherical projectiles. Lastly, ray-tracing simulations of various RCCs of known materials are provided to support the ongoing research on optical reflectance distributions with known shapes and to highlight how this may modify the current optical size estimation model. The status and plan forward are outlined for NASA's orbital debris shape effect investigation using a multidisciplinary approach by the ODPO and the HVIT team.

1. INTRODUCTION

The orbital debris environment is, by nature, dynamic and requires ongoing measurements to support environmental modeling and to assess the risks to space users from orbital debris. NASA's Orbital Debris Program Office (ODPO) continues to utilize ground-based optical, radar, and *in-situ* measurements to characterize the orbital debris environment and directly support engineering models, such as the Orbital Debris Engineering Model (ORDEM). Satellite designers and operators use ORDEM to help assess the orbital debris flux in various Earth orbits. ORDEM computes fluxes as a function of debris size, material density, impact speed, and direction along a mission orbit. In addition, ORDEM is used with NASA's Hypervelocity Impact Technology (HVIT) Bumper risk assessment tool to determine the orbital debris impact risk. Each ORDEM release provides more insight into the evolving environment by acquiring more recent measurement data, providing uncertainties in flux predictions, or by optimizing the architecture to meet broad-user needs.

With the evolving nature of spacecraft design and construction techniques, a new parameter is needed to help address risk assessments: shape. Characterizing shape has been an ongoing investigation, to understand shape-dependencies of radar cross section, optical signature variations from non-spherical targets, ground-based impact test shape binning, and more recently, the effect of shape (dependent on material) as it correlates to risk assessments. This paper will provide an overview of the shape categories used in ground-based hypervelocity impact experiments to assess the expected type of shapes that would result from an in-orbit breakup event and the distributions according to those categories. An overview of non-spherical projectiles used in hypervelocity experiments and hydrocode simulations will be presented. Additionally, ongoing work to model optical signatures using ray-tracing software to verify laboratory acquired measurement data will be highlighted.

2. SHAPE CATERGORIES: LABORATORY EXPERIMENTS

NASA and the Department of Defense (DOD) have collaborated for many years to utilize ground-based hypervelocity impact experiments to update and verify satellite breakup models. One of the first key laboratory experiments was conducted in 1992 using a fully functional 1960s era U.S. Navy Transit satellite. This laboratory test, the Satellite Orbital debris Characterization Impact Test (SOCIT), was designed to meet the criteria for a "catastrophic" collision. It produced more than 4700 fragments that were analyzed to determine their material, shape, and size distributions for comparison to breakup models used by NASA and DOD [1]. SOCIT used 10 shape categories: flat plate, curled plate, box, sphere, flake, rod, cylinder, box and plate, nugget, and other (irregular shapes not specific to any other shape bin). These shape categories were also used to determine how specific materials aligned with shape categories. For example, phenolic/plastic materials mostly broke into nugget or irregular shapes, as shown in Fig. 1. Aluminum fragments showed a broader shape distribution with nuggets, flakes, rods, curled plates, and the other category. It was documented that these material-shape characterizations were size dependent – understanding the correlation between fragment material, size, and shape is essential to better determine orbital debris risk to objects in orbit. Although SOCIT provided critical information used in updates to NASA and DOD breakup models, over time it was found the distribution of these fragment parameters was skewed in comparison to some on-orbit events [2, 3]. It was evident that with new materials and construction techniques, it was time to conduct another laboratory impact test that was representative of more modern satellites.

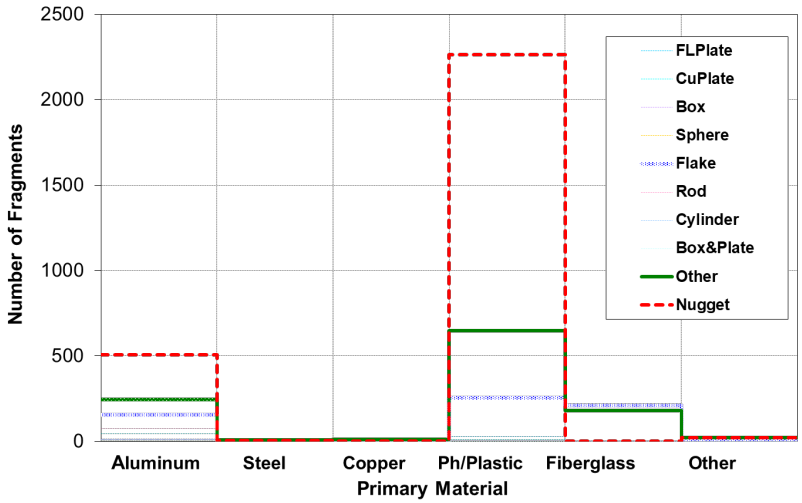

Fig. 1. Shape distribution from SOCIT [2]

DebriSat, a collaboration between the ODPO, the Space Force Space Systems Command (SSC), The Aerospace Corporation, and the University of Florida (UF), was designed in 2013 to replicate a high-fidelity, modern-day low Earth orbit spacecraft. The impact test was successfully conducted one year later, with the expectation that it would produce approximately 85,000 fragments measuring 2 mm or larger based on the NASA Standard Satellite Breakup Model (SSBM) [4]. At the current date, over 200,000 fragments have been collected and the number of fragments characterized continues to grow.

Using many lessons-learned for testing, characterization, and analysis from SOCIT, the DebriSat team worked closely with NASA's HVIT team to define shape rubrics that would be more useful for assigning fragments to a limited number of pre-defined shape categories. Like SOCIT, DebriSat focused on six primary shape categories: Flat Plate, Bent Plate, Straight Needle/Rod/Cylinder, Bent Needle/Rod/Cylinder, Parallelepiped/Nugget/Spheroid, and Flexible/multilayer insulation (MLI) [5]. The first five shape categories are similar to generalized classifications also used in SOCIT. The last category, Flexible, was introduced to capture new materials not used in former laboratory impact experiments (*i.e.*, MLI), which represents a category of materials and shapes that do not hold their shape or structure. The distribution of shapes from DebriSat as a function of cumulative number and size (characteristic length) scaled against NASA's SSBM is shown in Fig. 2. Details of the SSBM and its application to DebriSat are provided in [6]. The results, as of 01 January 2023, indicate that for fragments larger than approximately 2 cm, the dominant shape category is nuggets, like SOCIT. Unlike SOCIT, there is very limited use of phenolic or electrical potting materials in modern spacecraft, thus the nugget category is dominated by metallic fragments (aluminum, titanium, steel) at these larger sizes. A new material introduced in DebriSat is carbon fiber reinforced polymer (CFRP), a material that fragments primarily into two categories: plates and needles/straight rods. As shown in Fig. 2, the dominant shape for objects less than 2 cm is flat plates, followed closely by nuggets. Although the characterization and analysis of the DebriSat fragments are ongoing, the results to date have proven highly valuable in assessing the next steps for shape categorization and real-world applications, such as impact tests using non-spherical projectiles to assess the damage and ballistic limit equations (BLEs) for these new shape categories.

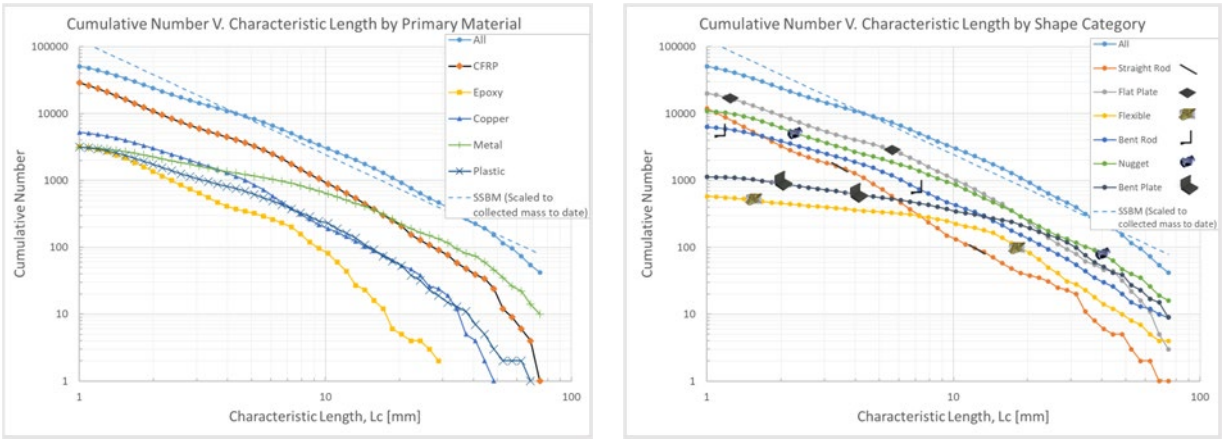

a) b)

Fig. 2. Shape distributions as a function of size, as of 01 January 2023, a) is DebriSat distribution as function of primary materials and b) is a distribution as function of shape

With ongoing efforts to use the distribution of fragments from both SOCIT and DebriSat to guide a series of hypervelocity impact tests, utilizing the 10 or even 6 shape categories was unreasonable and difficult, if not impossible, due to the challenges of using non-spherical projectiles in tests. To further simplify shape categories for testing and enable the comparison and extension of results through numerical simulations, the shape categories were assigned to three simple shape categories using right-circular cylinder approximations based on solid body dimensions. Tab. 1 shows how the solid body dimensions W1, W2, and W3 (provided by the fragment characterization) and bulk volume (V_{bulk} – total volume of solid material and voids) or solid body volume (V – mass divided by material density) can be used to simplify the shape categories into right circular cylinder (RCC) representations of plates, nuggets, or cylinders/rods [7]. Because the fragments are usually non-homogenous and irregularly shaped, V_{bulk} will be used here to remove any material density assumptions. This simplified approach allows using length-to-diameter ratios (L:D) to inform the size and shape of realistic non-spherical projectiles for impact testing and hydrocode simulations. Using this simplified approach, L:D can be used to inform the selection of size and shape of realistic non-spherical projectiles for impact testing and hydrocode simulations.

Tab. 1. RCC estimation for shape parameterization

Virtual RCC Dimensions	Flat Plate/ Flake/Flexible	Nugget/ Spheroid/ Parallelepiped	Straight Rod/ Needle/Cylinder
L	$\frac{4\,V}{\pi\,W_1\,W_2}$	W_2	W_1
D	$\sqrt{W_1\,W_2}$	$\sqrt{\frac{4\,V}{\pi\,W_2}}$	$\sqrt{\frac{4\,V}{\pi\,W_1}}$
L:D	$\frac{4\,V}{\pi}(W_1\,W_2)^{-\frac{3}{2}}$	$\sqrt{\frac{\pi\,W_2^3}{4\,V}}$	$\sqrt{\frac{\pi\,W_1^3}{4\,V}}$

The current version of the NASA SSBM used for building the ORDEM environment features three density groups: low density (LD, $\rho < 2$ g/cm^3), medium density (MD, $2 \leq \rho \leq 6$ g/cm^3), and high density (HD, $\rho > 6$ g/cm^3). With the addition of modern materials, a new category has been proposed for the ultra-low-density materials, specifically for fiber reinforced polymers like CFRP. Similar to variations in the specifics of most spacecraft materials, the design and build-up of CFRP can vary. A generally accepted density of 1.55 g/cm^3 is used when modeling CFRP in various tools used by the ODPO and HVIT. The L:D distributions of the current four density categories are presented in Fig. 3 using the three RCC shape bins. The corresponding peaks for these L:D distributions are shown in Tab. 2.

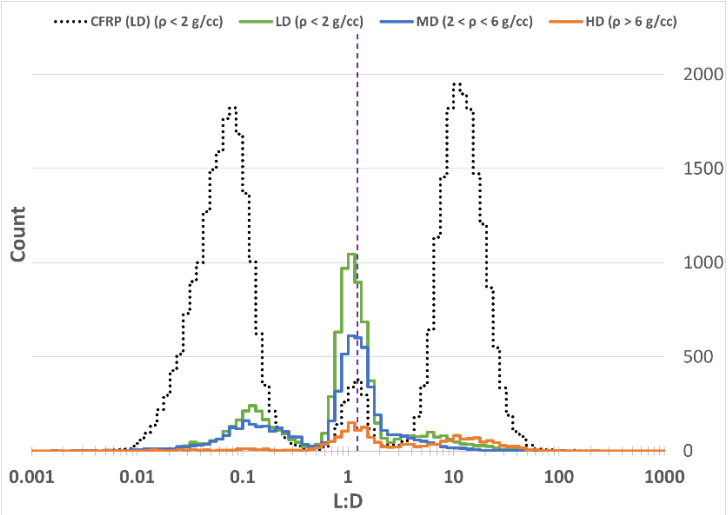

Fig. 3. L:D distribution for DebriSat fragments as of 01 January 2023

For plates, the peak L:D ratio is around 1:8, except for CFRP plates, which tend to be in the more extreme category, L:D = 1:13. For nuggets or spheroids, the peak L:D is 1:1 as expected. For rods/cylinders, the CFRP also dominates this shape category, but shares a peak L:D ratio with HD of 12:1. The peak LD and MD L:D are similar at 6:1 and 3:1, respectively, although a precise peak for MD rods/cylinders is not well observed. Using these L:D ratios for specific shape categories provides guidance for the range of projectile sizes/shapes to utilize for impact experiments and supporting hydrocode simulations, specifically using rod-like and plate-like projectiles.

Tab. 2. L:D peaks for DebriSat fragment distribution using RCC approximation as of 01 January 2023

Density Category	Plates/Flakes	Nuggets/ Spheroid/ Parallelepiped	Rods /Needles/ Cylinders
	V_{bulk}	V_{bulk}	V_{bulk}
CFRP	1:13	1:1	12:1
LD	1:7	1:1	6:1
MD	1:9	1:1	3:1
HD	1:9	1:1	12:1

3. NON-SPHERICAL PROJECTILES SHAPE STUDY

The HVIT group has developed and evaluated spacecraft micrometeoroid and orbital debris (MMOD) shielding for spacecraft (crewed and non-crewed) and designed operational techniques to reduce MMOD risk for over 30 years [8]. The team assesses MMOD risk to NASA missions using Bumper code and the latest version of the ODPO's ORDEM and NASA's Meteoroid Environment Office (MEO) Meteoroid Environment Model. Bumper code evaluates risk for spacecraft based on BLEs developed from results of laboratory impact experiments and hydrocode simulations. During the review process for ORDEM 3.0 and Bumper, the National Research Council (NRC) and NASA Engineering and Safety Center (NESC) both recommended the inclusion of shape effects into future versions of these models and tools. Specifically, the NRC 2011 Report recommendation stated that the ODPO's next version of ORDEM should be released as often as feasible to account for major changes to the environment or improved characterization of the orbital debris environment, including characterization of debris shape, as applicable. The NESC 2017 Report recommended that the ODPO and HVIT should use laboratory hypervelocity impact test data (*e.g.*, SOCIT, DebriSat) and other possible data sources to categorize debris shapes and define the relationship between characteristic length and mass/shape, incorporating this relationship into ORDEM 3.0 and Bumper to determine MMOD risk. NASA's HVIT group conducted preliminary studies of graphite-epoxy projectile shape on ballistic limits of high-risk areas on the International Space Station (ISS) in U.S. Government Fiscal Year (FY) 2018. The following year, NASA's Office of Safety and Mission Assurance provided the funding to continue HVIT assessments of non-spherical debris that would directly benefit the development of the next ORDEM release. A protection working group within the Interagency Debris Coordination Committee (IADC) provides international participation to evaluate the effects of projectile shape on spacecraft BLEs in recognition of this important space safety topic. Section 3.1 of this paper will provide an overview of hypervelocity impact tests conducted to date using non-spherical projectiles, and Section 3.2 will provide highlights of hydrocode simulations with non-spherical projectiles. Both methodologies are required to evaluate MMOD shape effect on spacecraft BLEs as discussed below.

3.1. HYPERVELOCITY IMPACT TESTS

The HVIT group, in coordination with the ODPO and the Remote Hypervelocity Test Laboratory (RHTL) at the NASA White Sands Test Facility in Las Cruces, New Mexico, have developed techniques to accelerate non-spherical projectiles reliably to approximately 7 km/s and analyze the precise orientation of the projectile at impact on experimental coupons. These impacts tests accelerate RCC projectiles using one of RHTL's two, two-stage, light-gas-guns (LGG). The larger LGG has a 0.50-caliber launch tube configuration, and the smaller LGG, shown in Fig. 4, has a 0.17-caliber. In both cases, the LGG uses a highly pressurized and hot hydrogen gas (out of view in Fig. 4a) to drive a sabot-encapsulated projectile to approximately orbital speeds.

These projectiles are separated from the sabot as they enter the target tank, Fig. 4a, where they proceed to the target, Fig. 4b. Specialized cameras (left and right in Fig. 4a) are used to image the projectile and determine its precise state and orientation at impact, and to image the impact ejecta and debris cloud (impact debris that passes through the coupon/shield wall) for multi-wall shields like the classic Whipple shield. A summary of the types of targets considered for this current study is given in Tab. 3.

Previously, the categories of shield types have focused on either operating spacecraft risk drivers or generalizable shield types that will form the foundation of generalized equations not specific to any vehicle. The three ISS risk drivers are a basic double-wall (Whipple) shield with a thermal blanket, an alumina-enhanced-thermal-barrier (AETB) and a space-proprietary-ablator-material (SPAM), which are both highly exposed reentry thermal protection materials that appear on visiting vehicles to the ISS. In addition to these ISS risk drivers, generalized studies have been performed on double-wall (Whipple) shields, monolithic plate material (single-wall shields) and MMOD enhanced thermal blankets (adaptive multi-shock shields).

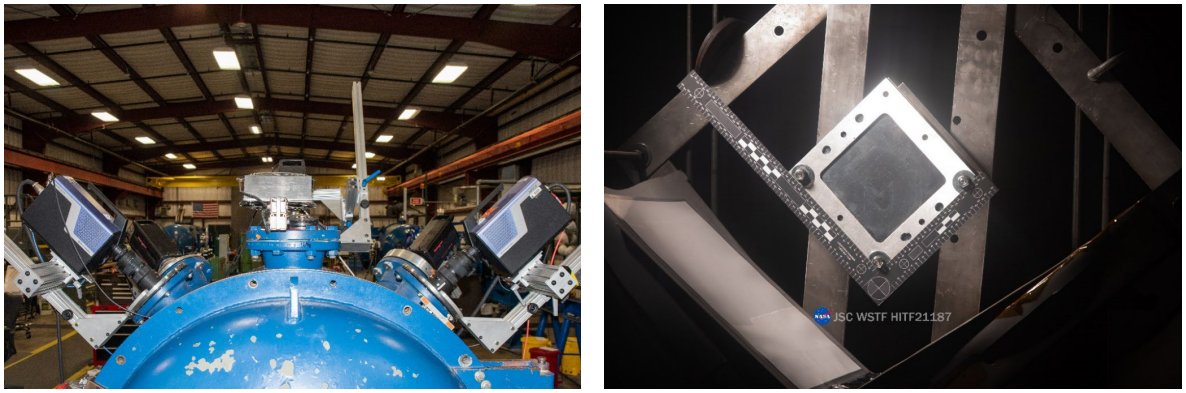

a) b)

Fig. 4. NASA White Sands Test Facility a) representative diagnostic configuration on target tank and b) view of the target from near the barrel

As can be seen in Tab. 3, a total of 75 shots have been performed to provide anchoring data for various shield categories commonly used in orbital flight. Each of the targets are placed in the target mounting fixture shown in the center of Fig. 4b and imaged throughout the impact. Fig. 5 shows images of a set of representative RCC projectiles. Fig. 5a and Fig. 5b show CFRP projectiles where the aspect ratios are approximately 3:1 and 1:3, respectively. Fig. 5c shows a copper RCC with the approximate aspect ratio of 3:1, and Fig. 5d shows a steel RCC with the approximate aspect ratio of 1:3.

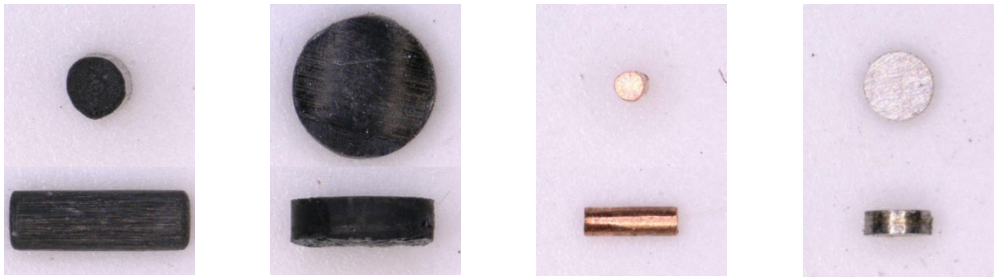

a) b) c) d)

Fig. 5. Representative images of RCC projectiles a) CFRP with L:D~3:1 b) CFRP with L:D~1:3 c) copper with L:D~3:1 and d) stainless steel with L:D~1:3

Tab. 3. Shape effect experiments of shield types performed to anchor numerical simulations.
*Number of all shots performed as of 30 June 2023

Shield Type	Shield Category	Number of Shots*	Projectile Types	L:D
Aluminum Whipple shield with MLI thermal blanket (Key ISS risk driver)	Double Wall Shield	26	CFRP Steel Copper	1:5 1:3 2:3 3:1
Aluminum Whipple shield (common structural shield)	Double Wall Shield	9	CFRP Steel Copper	1:3 2:3 3:1
MLI Whipple shield (common ultra-light weight shield)	Double Wall Shield	8	CFRP Steel Copper	1:3 3:1
Aluminum plate (common structural material)	Monolithic Shield	4	CFRP Steel Copper	1:3 3:1
Ti6Al4V plate (common structural material)	Monolithic Shield	5	CFRP Steel Copper	1:3 2:3 3:1
Steel plate (common structural material)	Monolithic Shield	2	Steel Copper	1:3 3:1
Copper plate (common electrical conductor)	Monolithic Shield	2	Steel Copper	1:3 3:1
Alumina-enhanced-thermal-barrier (thermal protection material)	Porous Monolithic Shield	10	CFRP Steel Copper	1:3 2:3 3:1
Space-proprietary-ablator-material (thermal protection material)	Porous Monolithic Shield	5	CFRP Steel Copper	1:3 2:3 3:1
MMOD enhanced thermal blanket (adaptive blanket for spot protection of critical structure)	Multi-shock Shield	4	Steel Copper	1:3 3:1

Double-wall (Whipple) shields are the most extensively used shield type that NASA currently assesses for spacecraft reliability and survivability assessments and have been widely studied for spherical projectiles [9]. This configuration allows spreading of debris clouds between the first wall (bumper) and rear (shield) walls; a much lighter wall is necessary to shield against a given projectile than for a single-wall shield, resulting in an overall lower-mass shield system. In general, it has been observed that the spherical shape of the projectile assists the spread of material through two mechanisms. First, the spherical shape is the most concentrated mass (meaning more of the projectile will see a strong shock wave); second, the spherical shape helps spread debris because of divergent shock waves in the bumper and reflecting shock waves from the curved rear surface of the projectile. Owing to the shear prevalence of this shield type and its potential loss of these benefits for non-spherical projectiles, this shield was studied extensively during these initial efforts to quantify performance of shields against non-spherical projectiles as shown in Tab. 3.

A representative array of images into a double-wall (Whipple) shield with a 0.5 mm thick Al6061-T6 bumper, 1.5 cm vacuum gap, and 2.0 mm thick Al6061-T6 rear wall is shown in Fig. 6. This figure shows an under-sampled array from one of the cameras of Fig. 1a with 0.4 ms between frames from just prior to impact to approximately 3 ms after initial impact. In these views, the trapped bumper material is in the left third of the images, and the rear wall is just visible at the far right of the images. The space between the bumper and rear wall is the expansion gap that allows the continuous diagnosis of the expansion process of the debris cloud.

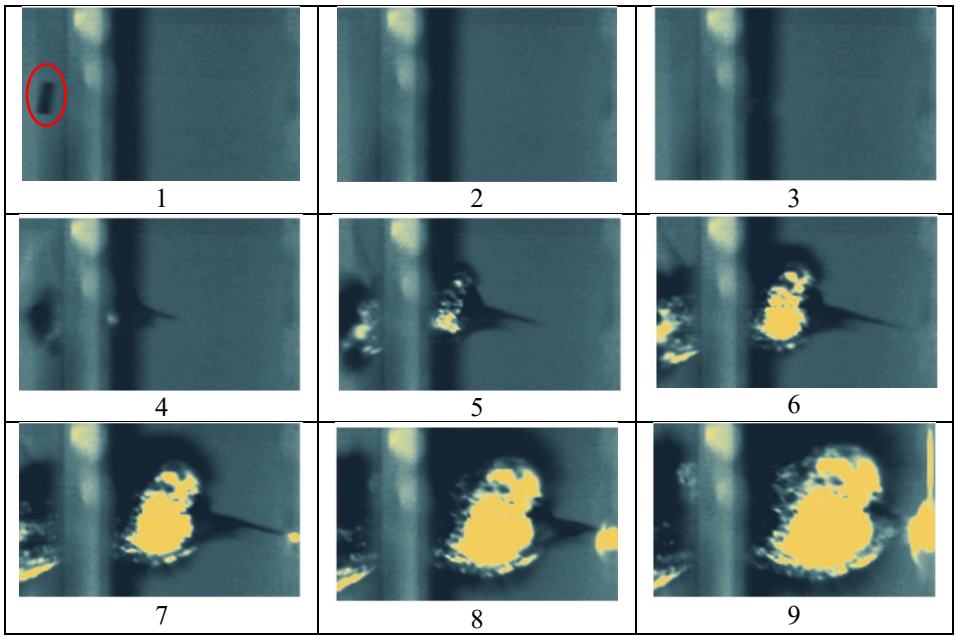

Fig. 6. Sequence of images at 0.4 ms intervals from the impact of a CFRP projectile with aspect ratio of approximately 1:3 from just prior to impact to approximately 3 ms after impact showing the evolution of the debris cloud. The projectile is circled in red in first frame in the test sequence.

This sequence of images is from the demise of the projectile shown in Fig. 5b (CFRP plate-like/disc-like projectile). As can be seen in the first frame of Fig. 6, the intact projectile's image is clearly caught prior to impact, and along with the other orthogonal camera images (not shown), these cameras allow the precise determination of the cylindrical axis orientation. The projectile's true dimensions and speed for this sequence are 0.671 mm length × 2.402 mm diameter and 6.99 km/s, respectively, and the projectile's central axis is pitched 10.3° from the velocity vector.

While the cameras are primarily used for determining the orientation of the projectile prior to impact, they also yield detailed information on the debris cloud expansion for comparison to numerical simulations. The first impact occurs at approximately the second frame of the figure, which is 0.4 ms after the first frame. The thickness of the trapping frames for the bumper obscures the view of this initial impact and earliest release of debris as seen in the second and third frames (approximately 0.4 ms after impact). Starting in the fourth frame, the debris cloud escapes the shadow of the bumper trapping, and a very high-speed mass of material jets out in front of the bulk of the debris cloud. This jet continues to outpace the rest of the debris as seen in the fifth, sixth, and seventh frames. From the video, the jet's speed is estimated to be about 10 km/s, over 40% faster than the projectile's initial speed and almost twice as fast as the bulk of the debris cloud, which is moving at approximately 5.5 km/s. The brightest region through frame 7 is a reflection of the light source off the debris cloud; however, after the debris starts to hit the rear wall, the self-emission of the shocked vapor starts to further oversaturate the camera.

In addition to the information from the cameras, the resulting damage to the shield walls is preserved following each shot. The residual damage to the shield walls resulting from this impact is shown in Fig. 7. The image in Fig. 7a is a micrograph of the front side of the bumper. As can be seen in the image, the projectile produced a very nearly circular hole with a diameter of 4.3 mm in the bumper. Like the bumper, the rear wall of the shield also survives the impact with the residual damage on the front side shown in Fig. 7b. As can be seen in the image, many fragmented solid impacts occurred over an approximate 3 cm diameter area. In addition, a small perforation occurred about half a centimeter from the center of impact in the location where the jet hit the rear wall.

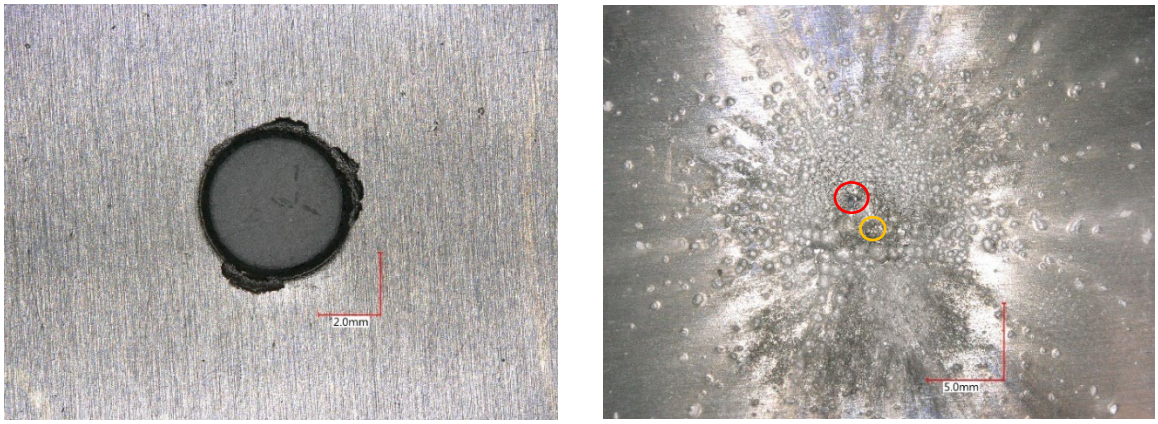

a) b)

Fig. 7. NASA White Sands Test Facility a) impact on front side of bumper shield and b) view of the target from near the barrel; the red circle represents primary impact and orange indicates the small perforation where the jet hit the rear wall

While this is just one example, it shows the scale of the information obtained during the development of hypervelocity impact verification data. This is repeated over and over for different shield types, but even these represent a fraction of the information needed to account for non-spherical projectiles. Along with the additional varied parameters of projectile types and L:D ratios, numerous sizes of projectiles, projectile orientation relative to the shield normal and velocity vector, impact speeds, and obliquities also need to be addressed. As can be imagined from this list, the parameter space exceeds what can be performed through experimental techniques and requires numerical simulations to explore a broad range of conditions.

3.2. HYDROCODE IMPACT SIMULATIONS

As discussed in Section 3.1, the parameter space for determining the ballistic performance of the wide array of shields in use in spaceflight is large, and the current database for spherical projectiles has been developed over decades. Expanding the field to incorporate non-spherical projectiles for the array of shields that required years of research using testing alone is not feasible. Moreover, the non-spherical nature introduces multiple new parameters as illustrated in Fig. 8. In addition to introducing multiple new parameters, the study of impact by non-spherical projectiles requires methods that are still maturing.

In Fig. 8a, a spherical projectile looks the same along the velocity vector and the shield surface normal vector regardless of orientation of the sphere; therefore, all that needs to be accounted for is the obliquity or angle between the projectile velocity vector and the shield surface normal vector. Observing the RCC in Fig. 8b, this rotation independence is not present for non-spherical projectiles. Further, this rotation independence is not the only complicating factor, as the aspect ratio can capture a range of values. To properly account for non-spherical projectiles, the parameter space increases by at least a power of three. This increase would be difficult to address with testing alone, and testing does not allow for fine control of variables like orientation, which would increase the need to duplicate tests. As a result of these factors, non-spherical shield studies cannot be performed in the traditional way of developing models through test alone and must rely on hydrodynamic simulations to develop models.

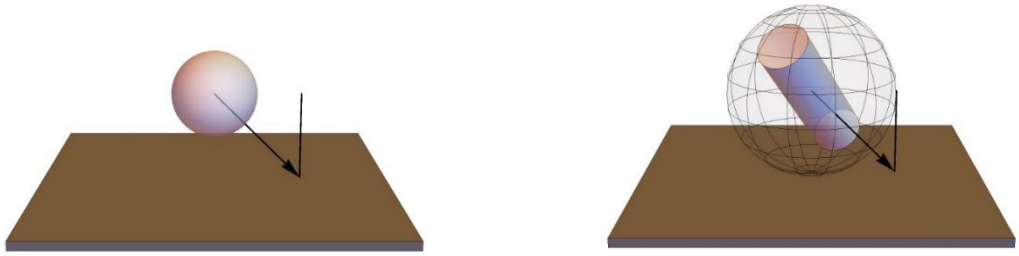

a) b)

Fig. 8. Illustration of an oblique impact of a projectile on a shield a) spherical and b) non-spherical RCC

Hydrodynamic simulations are performed with what are colloquially known as “hydrocodes”: multi-dimensional, nonlinear, structural-dynamics, continuum-analysis codes. These codes explicitly solve an initial value problem using the partial differential equations of motion (conservation of mass, momentum, and energy) with material closure models to predict the end state of a system after an amount of time passes (usually on the order of a tenth of a millisecond for spaceflight applications). These codes come in many forms, but generally fall into Eulerian methods where mass moves through a fixed space, or a Lagrangian method where a fixed mass is followed as it moves and distorts through space. Each of these techniques has its own benefits and drawbacks, but smooth-particle-hydrodynamics (SPH), which is a modified Lagrangian approach without a mesh, has been selected for this non-spherical work. The SPH tool being used by HVIT is a codeveloped Norwegian and French export-controlled code known as IMPETUS-γSPH [10]. The ability to track discretized mass yields faster simulations, while the meshless nature of the tool allows for addressing large distortions typical of hypervelocity impacts. While the techniques for interactions have been largely built into IMPETUS-γSPH, the response of materials is still greatly dependent on user-supplied models; hence, the need for checking results against actual experimental conditions. The 75 shots of Tab. 3 fill this purpose.

It is important to have good comparisons between simulations and actual experimental impact damage before proceeding with simulations that extrapolate to MMOD impact velocities that are not realized by experiment. Comparisons between simulation and experiment are made for the hole sizes in the bumper and rear wall layers as well as the permanent deformation of the rear wall. These comparisons have been made as described by the references [7, 11].

Fig. 9 provides the BLEs used in the MMOD risk assessments for the shield described in Section 3.1 (0.5 mm thick Al6061-T6 bumper, 1.5 cm vacuum gap, and 2.0 mm thick Al6061-T6 rear wall). The BLE gives the mass or size of projectile on the threshold of failure at the rear wall of the shield, where failure is defined as a through-hole, through-crack, or detached spall of the rear wall. Projectiles with mass equal to or greater than the curve are predicted to fail the shield; conversely, all projectiles with mass less than the BLE are expected to be stopped by the shield. The two curves represent the results for impact obliquities of 0° and 45°. The solid curves are for spherical projectiles, while the data points shown are the masses of non-spherical projectiles that have a 50% probability of penetrating the shield along with uncertainty estimates assuming a normal distribution. Each datapoint shown at 0° represents at least 3 sets of 5 simulations, and each datapoint shown at 45° represents at least 3 sets of 43 simulations demonstrating the large volume of simulation work to produce points like this. As can be seen, the mass with a 50% probability of causing the shield to fail is lower than the spherical counterpart which implies that for CFRP projectiles, the non-spherical shapes are more damaging on an equal mass basis than spherical projectiles. Therefore, an adjustment factor is required to bring down the modeled performance of the shield. Determining this factor to modify existing BLEs to match the simulated performance is the goal of this effort and requires analyzing many parameters and shield types to develop general engineering BLEs for non-spherical projectiles.

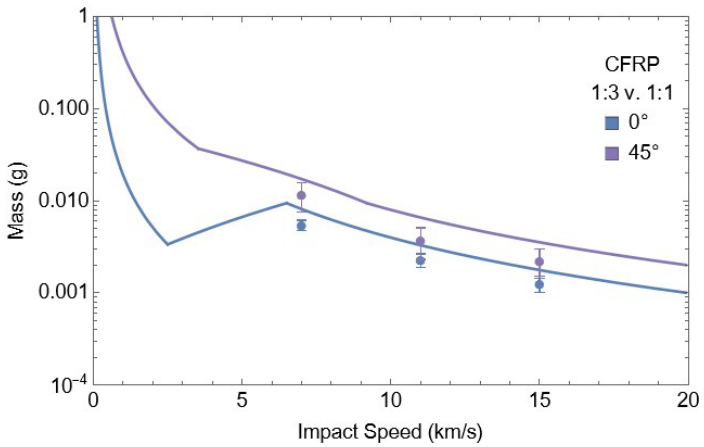

Fig. 9. Non-spherical ballistic limit simulated datapoints shown relative to existing spherical ballistic limit equation (solid curves) for impact obliquities of 0° and 45° to shield surface normal. Projectiles with masses below the curves are expected to be stopped by the shield.

Development of scale factors for many shield types and shield parameters is an on-going effort. To this point, over 3500 simulations have been performed in the last year and a half. This level of throughput is needed to derive the necessary adjustment factors for modeling the effects of non-spherical projectiles on the wide range of target configurations to positively inform spacecraft designs. In addition, the BLEs are an important component of tuning orbital debris model populations to observed small particle impact features on spacecraft radiator panels for instance; thus incorporating effects from non-spherical projectiles in these equations is key to capturing the effects of shapes within ORDEM. This work continues to move forward to develop projectile shape functions incorporating L:D to be applied to previously developed BLEs.

4. OPTICAL LABORATORY SHAPE INVESTIGATIONS

To further support measurement data used in ORDEM development, the ODPO continues to acquire measurements in its Optical Measurement Center (OMC). The OMC employs instrumentation that simulates telescopic observations to better characterize orbital debris and objects of interest in terms of photometric broadband measurements, light curves, phase functions, bidirectional reflectance distributions (BRDF), and spectral measurements. Details of the laboratory design, instrumentation, and data collected are available in [12-14]. These measurements will be used to update current optical size estimation models for debris populations based on ground-based telescope measurements for ORDEM; the effects of non-spherical shapes are thus of interest for characterizing shapes from optical measurements. Provided the complexities of the fragments generated from laboratory impact experiments such as DebriSat and SOCIT, similar to the use of hydrocode simulations for comparison to experimental tests, the ODPO team has focused on using ray-tracing optical software to simulate the light conditions in the OMC to analyze simple shapes and generate optical signatures of non-spherical shapes under controlled conditions. The following will highlight the analysis done on various shapes and materials.

To fully characterize a wide array of objects in the ray-tracing optical software in a manner that reflects the laboratory setup, scaled down versions of the xenon lamp light source and the camera/lens setup are recreated based on their physical analogs in the OMC. Any object with a specific size, shape, orientation, material, coating, and specular response can be created in the software with the option to import point clouds from actual 3-D scanned objects. To test the validity of the software, several simulation runs were completed using a simple calibration target: an aluminum sphere with a Lambertian surface (uniform reflectance in all directions). In the OMC, the aluminum sphere's light intensity is calculated by integrating the total reflected light captured by the camera. This same process is completed in the ray-tracing software for a simulated Lambertian-coated aluminum sphere at multiple phase angles, and the resultant phase functions from the two processes are compared. These phase functions, along with the modeled solution for an ideal Lambertian sphere are presented in Fig. 10a. The plots were scaled so that the first light intensity datapoint of each phase function is at 1, allowing for the comparison of the phase function slopes between measured, simulated, and modeled objects despite the differences in optical reflectivity. While the general trends of the phase functions are similar in all cases, the discrepancy between the measured Lambertian sphere and the simulated and

modeled spheres are likely attributable to the small defects on the surface of the measured Lambertian sphere used in the OMC caused by manufacturing and handling *versus* an ideal isotropic Lambertian sphere used in the simulations as discussed in [12].

After an initial validation, several shapes were then simulated to continue testing the capability of the software and enable the comparison of other measured objects in the OMC. In this process, a 1:1 aluminum plate and several aluminum cylinders with L:D ratios of 1:3, 3:1, and 3:2, all using Lambertian surfaces, were analyzed. The Lambertian plate was simulated with its face towards the camera, and the cylinders' orientations were such that the curved surfaces were facing the camera, as seen in Fig. 11 (right). These fixed orientations were used rather than the entire range of facet angles due to the current limitations of the simulation processing speeds related to the current workstation specifications. Improvements to the workstation are being implemented to speed up simulations that will also allow for more parameters to be implemented in the modeled measurements. The phase functions for each of these shapes, along with the modeled Lambertian phase function curve are shown in Fig. 10b. The cylinders' phase functions appear to show only small differences with a changing L:D ratio and follow the modeled Lambertian sphere phase function while the plate has a steeper slope at higher phase angles. Measurements of actual Lambertian cylinders and plates in the laboratory with these L:D ratios are necessary to validate these trends.

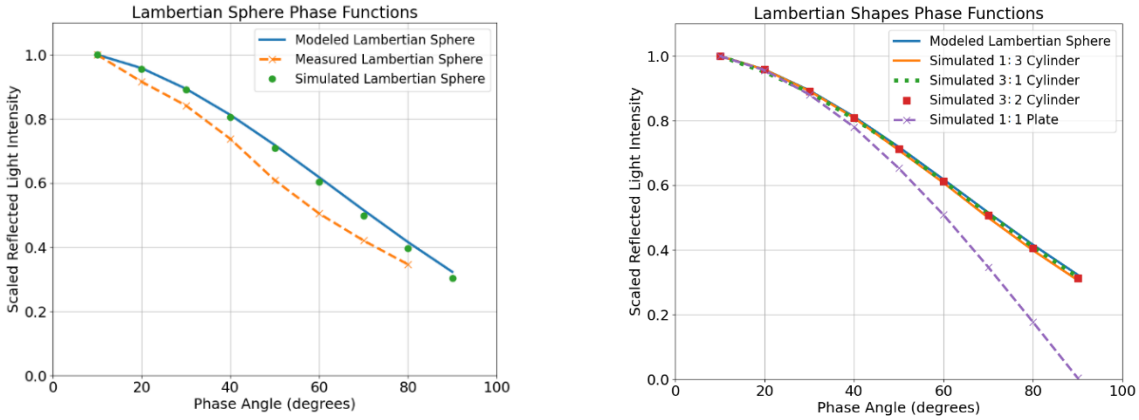

a) b)

Fig. 10. a) Phase angle plot of modeled, measured, and ray-trace simulated Lambertian spheres with their scaled light intensities b) Phase angle plot of a modeled Lambertian sphere compared to ray-trace generated simulated Lambertian shapes with various L:D ratios, specifically cylinders and a plate

A cylindrical telescope housing fragment from DebriSat was previously measured in the lab (see Fig. 11 for CCD and simulated images), and its corresponding phase function was analyzed in comparison to a simulated 3:2 Lambertian cylinder and a modeled lunar sphere shown in Fig. 12. It is important to choose materials and scatter models in the ray-tracing software that most closely resemble an object's optical characteristics, a fact highlighted by two factors: 1) the difference between the phase functions of the simulated 3:2 Lambertian cylinder and the telescope fragment and 2) the similarity in phase function slope of the modeled solution of an ideal lunar sphere and the measured telescope fragment.

Further measurements and simulations are being conducted to investigate the effects of applied scatter models on the phase functions, and a preliminary qualitative comparison of an aluminum sphere with an applied Harvey-Shack scatter model to measurements of a semi-specular aluminum sphere at multiple phase angles as illustrated in Fig. 13[15]. Several other scatter models, including a Phong BRDF, have also been applied and tested on several shapes [16].

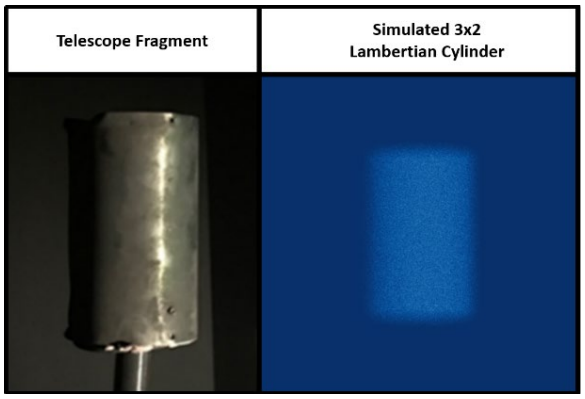

Fig. 11. (left) A CCD image of a cylindrical telescope fragment (right) A simulated 3:2 Lambertian cylinder in a ray-tracing software.

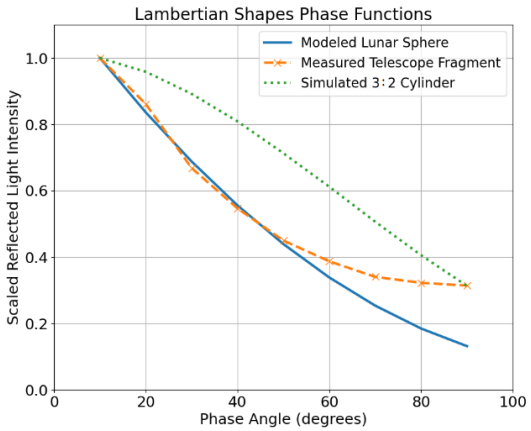

Fig. 12. Phase angle plot of a measured telescope fragment, a ray-trace simulated 3:2 cylinder, and a modeled lunar sphere for comparison

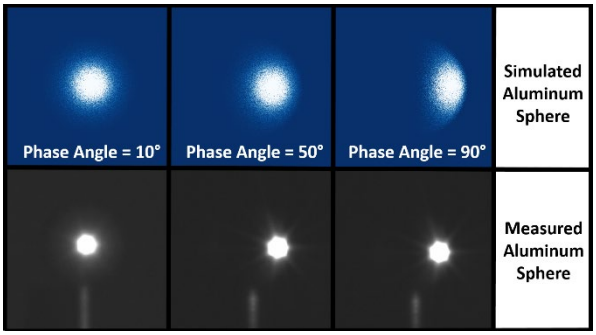

Fig. 13. (top) A simulated aluminum sphere with a Harvey-Shack BRDF applied, at multiple phase angles (bottom) Images of a semi-specular aluminum sphere taken in the OMC at multiple phase angles

5. CONCLUSIONS

This paper has highlighted the various avenues of research being conducted by NASA to investigate shape effects of orbital debris and the implementation of a shape parameter into future models of the orbital debris environment. For ORDEM, the data used to build the model relies on the latest optical, radar, and *in-situ* measurements. Utilizing recent laboratory impact tests provides direct measurements that can be used to characterize the distribution of shapes in terms of cumulative numbers, associated materials/material densities and sizes. DebriSat and SOCIT have provided critical information on characterizing these fragment distributions using classical and modern representative LEO spacecraft.

Building on these laboratory impact tests, the ODPO and HVIT team have been working in coordination to understand the risk from non-spherical projectiles using laboratory impact tests and simulations. Accounting for the large number of parameters needed to analyze the damage from non-spherical projectiles, hydrodynamic simulations provide a means to extend laboratory impact tests and better assess the damage on specific shields in a specified environment.

In addition, ODPO has investigated improvements to the current size estimation model used to convert optical magnitudes to sizes from telescopic measurements for input into ORDEM. The ODPO continues to use the OMC to simulate telescopic data, but similar to the complexities of impact experiments, utilizing ray-tracing software allows the optical characterization to be evaluated in a controlled environment, accounting for its associated difficulties (*i.e.*, defining the appropriate surface material for simulations).

The shape study work presented has demonstrated the multi-disciplinary approach to assess shape as a new parameter to support ORDEM development and evaluate BLEs for various shields required to assess risk from MMOD.

6. REFERENCES

[1] P.H. Krisko, M. Horstman, M.L. Fudge. SOCIT4 collisional-breakup test data analysis: with shape and material characterization, *Adv. Space Res.*, 41(7): 1138-46, 2008.

[2] M. Matney. "Small Debris Observations from the Iridium 33/Cosmos 2251 Collision," Orbital Debris Quarterly News Volume 14 Issue 2, pp. 6-8, April 2010..

[3] J.-C. Liou and N. Johnson. "Physical Properties of the Large Fengyun-1C Breakup Fragments," Orbital Debris Quarterly News Volume 12 Issue 2, pp. 4-5, April 2008.

[4] N.L. Johnson, P.H. Krisko, *et al.* NASA's New Breakup Model of EVOLVE 4.0, *Adv. Space Res., 28*(9): 1377-1384, 2001.

[5] M. Rivero, *et al*. "DebriSat Fragment Characterization System and Processing Status," 67th International Astronautical Congress Proceedings, Guadalajara, Mexico, 2016.

[6] H. Cowardin, *et. al*. "Updates to the DebriSat Project in Support of Improving Breakup Models and Orbital Debris Risk Assessments," Proceedings of the 2019 Hypervelocity Impact Symposium. Destin, FL, April 14-19, 2019. HVIS2019-066.

[7] J. Miller, *et. al*. "Development of Experimental Techniques for Non-spherical Hypervelocity Impacts," Proceedings of the 2022 Hypervelocity Impact Symposium, Alexandria, VA, September 18-22, 2022.

[8] NASA Hypervelocity Impact Technology (HVIT) website: https://hvit.jsc.nasa.gov/

[9] Astromaterials Research and Exploration Science Directorate. Handbook for Designing MMOD Protection; Technical Report JSC-64399; NASA: Washington, DC, USA, 2009.

[10] A. Collé, *et al*. "An Accurate SPH Scheme for Hypervelocity Impact Modeling," Proceedings of the 2019 Hypervelocity Impact Symposium, Destin, FL, April 14-19, 2019. HVIS2019-078.

[11] J. E. Miller. "Study of the effect of a non-spherical projectile on Whipple shields," Second International Orbital Debris Conference, paper #6136 (pending), Houston, TX, December 2023.

[12] J. Hostetler and H. Cowardin. "Experimentally-Derived Bidirectional Reflectance Distribution Function Data in Support of the Orbital Debris Program Office," Proceedings of the 2019 AMOS Conference, Maui, Hawaii, September 2019.

[13] J. Hostetler and H. Cowardin. "Experimentally Derived Phase Function Approximations in Support of the Orbital Debris Program Office," First International Orbital Debris Conference, Houston, Texas, December 2019.

[14] H. Cowardin, *et al*. "Updates on the DebriSat Hypervelocity Experiment and characterization of Fragments in Support of Environmental Models," Proceedings of the 2022 Hypervelocity Impact Symposium. Alexandria, VA, September 18-22, 2022.

[15] K. Nattinger. "Experimental validation of the Generalized Harvey-Shack surface scatter theory", Proc. SPIE 11485, Reflection, Scattering, and Diffraction from Surfaces VII, 1148503 (20 August 2020); https://doi.org/10.1117/12.2568233

[16] B.-T. Phong. "Illumination for computer generated pictures," PhD thesis, The University of Utah, 1973.